NJC

Tuning the properties of boron-doped reduced graphene oxide by altering the boron content

Journal:	*New Journal of Chemistry*
Manuscript ID	NJ-ART-08-2020-003909.R1
Article Type:	Paper
Date Submitted by the Author:	14-Sep-2020
Complete List of Authors:	Ngidi, Nonjabulo; University of KwaZulu-Natal, School of Chemistry and Physics Ollengo, Moses; University of KwaZulu-Natal, Chemistry Nyamori, Vincent; University of KwaZulu-Natal, Chemistry

Tuning the properties of boron-doped reduced graphene oxide by altering the boron content

Nonjabulo P. D. Ngidi, Moses A. Ollengo, and Vincent O. Nyamori*

School of Chemistry and Physics, University of KwaZulu-Natal, Westville Campus, Private Bag X54001, Durban 4000, South Africa

*Corresponding author: Tel. +27-31-2608256, Fax: +27-31-2603091, Email: nyamori@ukzn.ac.za

Email addresses of co-authors: nonjabulongidi@gmail.com, mosesollengo@gmail.com

Abstract

The design and fabrication of electronic devices based on graphene nanomaterials are dependent on the tuning of Fermi levels. This can be achieved by doping graphene oxide (GO) with an electron-withdrawing (*p*-type) or electron-donating (*n*-type) species that causes changes in the electron density and enhances the electrochemical properties. In this research, the effect of boron content on the optical, electrochemical, and conductivity properties of GO was investigated. Boron-doped reduced graphene oxide (B-rGO) was synthesized *via* a chemical vapor deposition method by using GO and varying amounts of boric anhydride, as a boron precursor, at a doping temperature of 600 °C. The B-rGO samples were characterized by standard spectroscopic techniques. B-rGO had a sheet structure with various graphene islands and disordered regions. The highest boron content incorporated into the reduced GO framework was 7.12%. B-rGO samples manifested strong absorption in the ultraviolet region. An electronic band structure with a low charge resistance of 20.23 Ω and enhanced electrical conductivity properties of 5.920 S cm^{-1} was observed and noted to be dependent on the concentration of boron incorporated. All the B-rGO samples demonstrated a *p*-type conductivity behaviour which is attributed to an increase in the density of states near the Fermi level. This work opens a new avenue for the fabrication of solar cells based on *p*-type B-rGO.

Keywords

Reduced graphene oxide; boron-doped; chemical vapor deposition; electronic structure; electrochemical properties.

Correspondence

*Vincent O. Nyamori, School of Chemistry and Physics, University of KwaZulu-Natal, Westville Campus, Private Bag X54001, Durban, 4000, South Africa

Email: nyamori@ukzn.ac.za

1 Introduction

Graphene-based nanomaterials have been widely researched for different potential applications. It is of interest to understand how to modify their electronic structure, through the introduction of heteroatoms or the creation of defects, to fabricate suitable graphene-based materials with appropriate physical, chemical, and electronic properties [1]. The modification of the electronic structure of graphene causes electron modulation to tune its optoelectronic properties for a specific application, such as energy conversion and storage [2,3]. The modification of the carbon sp^2 lattice in graphene results in the formation of covalent bonds with functional groups or other molecules [4]. Exploratory and theoretical investigations on graphene doping demonstrate the possibility of synthesizing *p*- and *n*-type semiconductors *via* substitution of carbon with various heteroatoms in the graphene framework [5-8]. Thus, various heteroatoms have been doped into the graphene lattice, for example, nitrogen, boron, sulfur, phosphorus, and many different metals.

Boron is one of the heteroatoms that can initiate novel and complementary properties prompting specific applications in solar cells [9]. This is evident from DFT calculations that show that the boron atom can efficiently displace the carbon atom from the graphene lattice and that the energy barrier to dope a boron atom into the graphene lattice is lower than that of a nitrogen atom [10]. The boron atom is less electronegative than a carbon atom and, during doping, it induces a *p*-type conductivity in graphene [11]. Boron-doping in the graphene framework leads to redistribution of electron density, where the electron-deficient boron sites provide the enhanced binding capability. This occurs because when boron substitutes carbon in the hexagonal sp^2-bonded structure, it introduces holes as charge carriers which imposes a characteristic bandgap and produces excellent conductivity [2,12,13]. Jia *et al.* [14] reported a higher ratio of *sp*-hybridized carbon to sp^2-hybridized carbon (4:1) which has also showed excellent electrochemical electrode performance and enhanced photocatalytic properties.

In general, boron-doping is advantageous for various applications, such as supercapacitors [15], hydrogen storage [16], potassium-ion batteries [17,18], field emissions [19], gas sensing [20], photo- and heterogeneous-catalysis [21], biomedical applications [22], and solar cells [23]. To investigate the electronic properties of graphene-modified by boron-doping, the total density of state of boron-doped graphene oxide (B-GO) is used. Notably, the Fermi level (E_F) of graphene corresponds

with the Dirac point. Boron has one less electron than carbon, thus it can easily displace a carbon atom. Also, the close covalent atomic radii of 85 pm for boron and 70 pm for carbon allow boron to displace carbon even when the process is linked with a large activation energy barrier such as 2.6 – 2.8 eV [24,25]. This exchange occurs when the interlayer spacing (d_{002}) of epitaxial graphene is bigger, thus, the moire´ resulting from the overlaid epitaxial graphene and lattices imposes a potential, inducing Dirac cone replica and leads to the opening of the bandgap in the band structure [26,27]. The B-GO isomers that are formed from various chosen doping sites have been observed to differ in the bandgap, bond length, and stability [28]. The bandgap is observed to be at its greatest when dopants are placed at the same sublattice point of graphene because of the consolidated impact of the symmetrical breaking of sublattices. However, when the dopants are placed at adjacent sublattice positions, it results in a closed bandgap.

The two facets, bandgap, and *p*-type characteristics have been investigated mostly *via* experimental and theoretical approaches. In theoretical computations, boron-doping in a graphene lattice is assumed to substitute the carbon atom, resulting in two outcomes. Firstly, this introduces chirality in the basal plane, and at this point, bandgap oscillations vanish rapidly as a function of the chiral angle [29]. Secondly, carbon substitution by a single boron atom has the potential to induce spontaneous magnetization, independent of the site of substitution [24], arising from a spin polarization, and results in a lower bandgap near the Fermi energy [29,30]. The induced magnetic moment is localized at the substitution site [30,31].

Experimentally, boron-doping can be achieved by different approaches such as hydrothermal or solvothermal synthesis [32-34], high-temperature chemical vapor deposition (CVD) [35], and plasma treatment [36]. These techniques can also be divided into *in situ* and *ex situ* methods. Plasma treatment, which is an *in situ* approach, has been reported to be an efficient route for boron-doping. However, with this method, it is possible to increase the number of defects on the graphene-based nanomaterials, and this further attenuates its electrical conductivity. The issue with *in situ* approaches is that impurities from the metal catalyst precursors inhibit the investigation of the exclusive contribution from the doped material. On the other hand, in the case of *ex situ* approaches, there are also disadvantages, and this includes the requirement of very high temperatures and additional time or steps to obtain efficient boron-doped samples.

Hydrothermal and solvothermal approaches have been used in the synthesis of graphene-based materials, especially in boron-doped graphene. These approaches are performed in a sealed autoclave at temperatures exceeding the boiling points of organic solvents and are not time-consuming. Thermal exfoliation is also preferable because of its cost-effective, easier to scale-up, and produces large quantities of graphene [37,38]. CVD is a frequently used approach. However, the issue with the CVD method, is that during the doping process, the dopant precursors are not completely exhausted, hence, they may cause contamination and compromise the characteristic electrocatalytic properties. Therefore, purification is required; hot distilled water [2] can be used to remove excess or unreacted boron precursors from doped graphene. Alternatively, for large-scale purification, sodium hydroxide [39], ethanol [40], or hydrochloric acid [15] can be used to remove boron precursors. Normally, NaOH is used because it is effective, easily available, and relatively easy to separate B_2O_3 in B-rGO. The CVD approach is carried out with a certain boron precursor at elevated temperatures [40]. When graphene oxide (GO) or reduced graphene oxide (rGO) are doped with boron, they tend to yield more complex structures such as boronic esters, borinic esters, and boronic acids [11]. The issue with boron-doping is to regulate the boron concentration, bonding configuration, and electron transport properties.

Panchakarla *et al*. [41] reported that a boron content of 2% tends to cause a Fermi level shift of 0.65 eV, exhibiting a *p*-type conductivity. Recently, studies on the synthesis of boron-doped reduced graphene oxide (B-rGO) have focused on the use of various boron precursors and methodologies. In 2016, Thirumal *et al.* [15] reported B-rGO with a doping content of 2.56% by using hydrothermal reduction of boric acid as a boron precursor. However, in 2018, Mannan *et al.* [33] used a similar method to synthesize B-rGO and achieved a boron content of between 1.64 and 1.89%. The difference in boron content was caused by the use of various reactants and reaction conditions (boron precursor, temperature, time, and pressure) during the boron-doping procedure. This suggests that different reactants and reaction conditions result a varying boron content in B-rGO.

In this paper, the conditions for the preparation of B-rGO were optimized, thus, GO was doped with varying amounts of boron (using boric anhydride, B_2O_3 as a precursor) at a doping temperature of 600 °C, by using the CVD approach. Boric anhydride has been widely reported

as a boron precursor and tends to results in better doping in graphene [33,42], thus, in this case, it was used. In literature, most of the synthesis of boron doping has been done in relatively higher doping temperatures such as 1200 °C [43], 1000 °C [3], and 700 °C [40]. Thus, the novelty of this work is based on the attempt to introduce different doping percentages in B-rGO at a relatively lower doping temperature and to determine how the different amounts of boron-doping affect the surface energy, and electrochemical, optical, and conductivity properties.

2 Experimental approach

2.1 Materials and instrumentation

Boric anhydride (B_2O_3, ≥98%), a boron standard solution (9995 mg ± 20 mg L^{-1}), graphite powder (99.99% trace metal basis), and sodium hydroxide (NaOH, ≥97%) were purchased from Sigma-Aldrich, South Africa. A gas mixture of 10% hydrogen in argon (v/v) was purchased from Afrox Limited Gas Company, South Africa. A digital ultrasonic water bath (400 W), which was supplied by Shalom Laboratory Supplies, South Africa, was used for sonication. Double distilled water was obtained from a double distiller (Glass Chem water distiller model Ws4lcd, supplied by Shalom Laboratory Supplies, South Africa).

2.2 Synthesis of B-rGO

GO was synthesized by a modified Hummers' method [44]. B-rGO was synthesized through thermal annealing of GO in the presence of various amounts of B_2O_3. The doping temperature was varied (600, 700, and 800 °C) during the synthesis, and a doping temperature of 600 °C was found to be the optimum doping temperature for B-rGO, thus this article focuses on 600 °C. The synthesis at 600 °C was performed in triplicate. In a typical procedure, GO was first mixed mechanically with different masses of B_2O_3 (40, 50, 60, and 70 *wt.*%, which herein are denoted as B-rGO-40, B-rGO-50, B-rGO-60, and B-rGO-70, respectively). After mechanical mixing, the mixture was transferred into a corundum crucible and, thereafter, placed in the centre of a quartz tube (length 850 mm, inner diameter 27 mm) under a continuous flow of 10% hydrogen in argon. The heating system used was a tube furnace (Elite Thermal Systems Ltd., TSH12/50/610) fitted with a temperature controller (Eurotherm 2416). The furnace was heated from room temperature to 600 °C at an increasing rate of 10 °C min^{-1}. After the furnace had reached 600 °C, the temperature was held constant for two hours, and, thereafter, the sample was allowed to cool naturally to room temperature under an argon atmosphere. For

purification, the product obtained (0.5 g) was refluxed at a temperature of 100 °C in a 3 M NaOH aqueous solution for two hours to remove unreacted B_2O_3. The sample was then filtered through a sintered glass funnel under vacuum and washed with double distilled water. Thereafter, the product was dried in an oven at 60 °C for 24 hours. Then, FTIR spectroscopy was used to verify that all the unreacted B_2O_3 had been successfully removed

2.3 Characterization

The surface morphology of the synthesized B-rGO was characterized by a field emission scanning electron microscope (FE-SEM, Carl Zeiss Ultra Plus). Further morphological and structural characterizations were performed with a high-resolution transmission electron microscope (HR-TEM, JOEL JEM model 1010). A Fourier transform infrared spectrophotometer (FTIR, PerkinElmer Spectrum 100) equipped with an attenuated total reflection (ATR) accessory was used to investigate the presence of various functional groups in B-rGO. Briefly, the sample, B-rGO, was pressed into a pellet under a pressure of 10 Tons and thereafter placed on a diamond crystal for analysis. In the case of Raman spectroscopy, a DeltaNu Advantage 532™ Raman spectrophotometer, with an excitation source of a Nd:YAG solid-state crystal class 3b diode, was used to determine the graphitic nature or crystallinity of B-rGO. The excitation wavelength (λ) was 514.5 nm, and Nuspec™ software was used to generate the Raman spectra.

The boron content in B-rGO was determined by electron dispersive X-ray spectroscopy (EDS, Oxford instrument - INCA 4.15) and inductively coupled plasma-optical emission spectrometry (ICP-OES, PerkinElmer Optima 5300 DV). Briefly, 10 mg of each B-rGO sample was digested in a mixture of 30% (v/v) hydrogen peroxide and concentrated sulfuric acid (ratio 3:1, respectively) until the black solid of B-rGO dissolved. The digested mixture was quantitatively transferred to a 100 mL volumetric flask and the solution was made up to the mark with double distilled water. Standard solutions of boron were prepared with different concentrations, i.e. 10, 20, 30, 40, 50, 60, 70, 80, 90, and 100 mg L^{-1}, from a commercial boron standard solution. All the standard solutions and B-rGO samples were filtered through 0.45 μm syringe filters and transferred into ICP vials for analysis.

The surface area and porosity (textural characteristics) of the samples were investigated with a Micromeritics TriStar II 3020 analyzer. Approximately 0.2 g of B-rGO was degassed for 1 h at 90 °C, after which the temperature was raised to 160 °C and further degassed for 12 h in a Micromeritics Vacprep 061 sample degassing system. After degassing, the B-rGO samples were fitted in the Micromeritics TriStar II instrument. The pore volumes were obtained with the Barrett-Joyner-Halenda (BJH) model, while the specific surface area was calculated with the Brunauer–Emmett–Teller (BET) isothermal model.

Thermal stability was investigated using a TA Instruments Q Series^{TM} thermal analysis instrument (DSC/TGA (SDT-Q600)). The B-rGO samples were heated from ambient temperature to 1000 °C at a rate of 10 °C min^{-1} under airflow. X-ray powder diffraction (XRD, Rigaku/Dmax RB) was used to investigate the phase composition of B-rGO with graphite monochromated high-intensity Cu K_{α} radiation (λ = 0.154 nm) and a θ-θ scan in a locked coupled-mode. Optical properties were determined with a UV-Visible spectrophotometer (Shimadzu, UV-Vis-1800). The GO and B-rGO samples were first dispersed in absolute ethanol and then sonicated for 30 min before analysis. A PerkinElmer LS 55 spectrofluorometer fitted with a solid sample accessory was used to investigate the charge recombination of B-rGO. Excitation was performed at 310 nm, and the emission spectrum was recorded from 450 to 550 nm with the excitation slit and emission slit set at 5 nm and 2 nm, respectively.

Electrical conductivity was determined from four-point probe measurements using a Keithley 2400 source-meter. The B-rGO samples were first formed into a pellet with a thickness of 0.02 mm. Cyclic voltammetry (CV) was conducted on a Metrohm 797 VA Computrace electrochemical workstation with a 57970110-dosing processor potentiostat (Metrohm, Switzerland). Electrochemical impedance spectroscopy (EIS, CHI 600E work station, CHI Instruments) was used to determine the electrochemical properties of B-rGO. A three electrode system was used, namely, a counter electrode (platinum wire, Pt), reference electrode (Ag/AgCl), and working electrode which was prepared by casting the B-rGO sample onto a glassy carbon electrode. A ferro/ferricyanide ($[Fe(CN)6]^{3-/4-}$) redox couple was used as the electrolyte. The CV was performed at a scan rate of 100 mV s^{-1} with a potential range from -0.4 to 0.6 V. The electrodes for electron impedance spectroscopy (EIS) were prepared similarly

and the impedance was measured in a frequency range of 1 – 1000 Hz with a potential amplitude of 10 mV s^{-1}.

3 Results and discussion

In this work GO and four samples of rGO doped with different amounts of boron were prepared and characterized.

3.1 Boron content

The ICP-OES and EDS (Table 1 and Supplementary data - Figure S1) were used to confirm the targeted boron wt.% for each B-rGO sample prepared. The boron concentrations determined from ICP-OES were used to further calculate the wt.% doping in the B-rGO. The boron content present in B-rGO was quite low relative to the targeted boron wt.%, this is because the replacement of a carbon atom with a boron atom is difficult. The boron content present in B-rGO was found to be between 3.36 and 7.12%, and this followed the trend of the wt.% of boron precursor (boric anhydride) used. For example, sample B-rGO-70 which had the highest amount of boric anhydride provided the highest percentage of boron from ICP-OES analysis, whilst B-rGO-40, with the least wt.% of the boron precursor, gave the lowest readings. With this clear trend, it is, therefore, possible to tune the boron concentration of the synthesized B-rGO samples by varying the amount of boron precursor used.

Table 1: Quantitative analysis of boron in B-rGO samples

Sample	Boron/(m/m)%
GO	-
B-rGO-70	7.12 ± 0.4
B-rGO-60	5.98 ± 1.1
B-rGO-50	4.60 ± 0.4
B-rGO-40	3.36 ± 0.1

3.2 Functional groups

Figure 1 shows the FTIR spectra of GO and B-rGO in the range of 200 – 4000 cm^{-1}. In Figure 1 (a) it is seen that at least five peaks in the spectrum of GO show distinctive characteristics. The five characteristic peaks were observed at 1051, 1240, 1615, 1750, and 3250 cm^{-1}, which are assigned to the stretching vibration of alkoxy (C-O), epoxy (C-O-C), aromatic (C=C), carbonyl (C-O), and hydroxyl (OH) groups, respectively [45-47]. However, after boron-doping, the hydroxyl peak became sharper and is shifted from 3250 cm^{-1} to 3150 cm^{-1} due to the consequent reduction of GO and incorporation of boron atoms into the GO lattice. Other new peaks were observed at 1102, 1180, and 1383 cm^{-1} which were attributed to the stretching vibration of C-O, B-C, and B-O bonds, respectively [33,48].

Since boron is less electronegative than carbon, it tends to act as an electron acceptor in the vicinity of C-B bonds. The bond length of boron-boron is equal to 1.56 Å at 300-1000 K. Therefore, it is 10% longer than the carbon-carbon bond (1.41 Å). As a result, certain perturbations of the honeycomb framework of graphene are unavoidable. Thus, the position in which the dopant atoms are situated is very important, because a higher symmetry of the nanostructure can reimburse for perturbation annoyances. The C-B bond length is 1.52 Å. There is a small difference in the electronegativity between carbon (2.55) and boron (2.04), therefore the bonds are expected to be weakly polar. The heat of formation indicates a change of enthalpy during the formation of one mole of the compound from its simple substances. Higher temperatures tend to enhance the heat of formation. The increase in heat of formation lowers the thermodynamic stability [49]. The covalent bond length between boron and carbon, and electron relaxing void introduced by boron (HOLE) by lowering the overall states, has the consequence of a slight red-shift as opposed to the expected blue-shift. Thus, from the spectral analyses, it can be suggested that boron functionalities have been incorporated into the GO network [33].

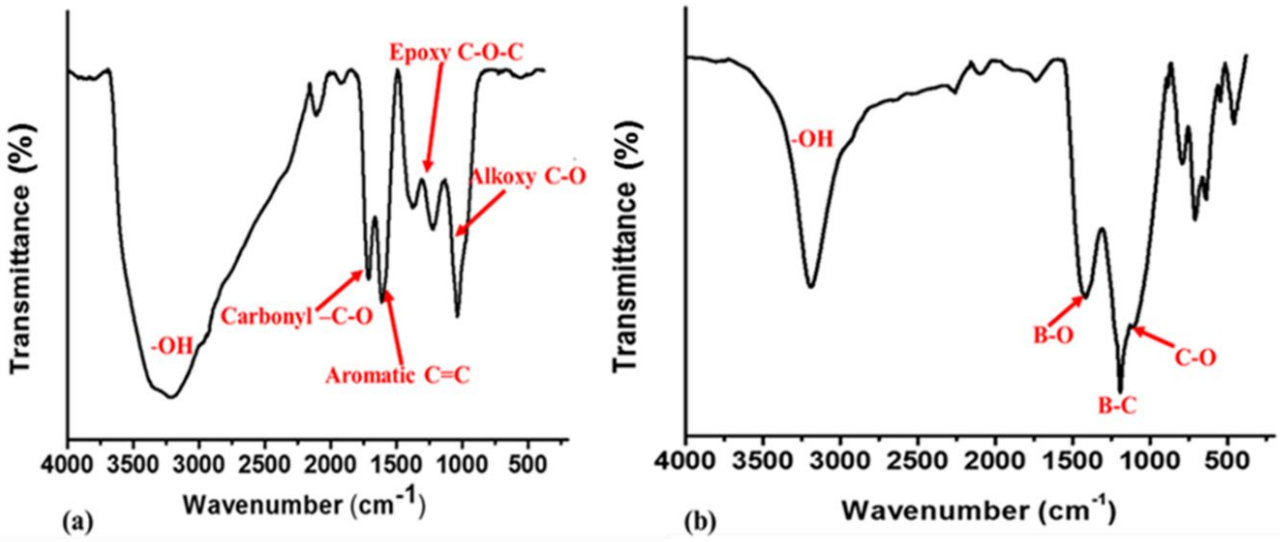

Figure 1: ATR-FTIR spectra of (a) GO and (b) B-rGO-40

3.3 Morphology

The 2-D structural morphologies of the B-rGO samples are shown in Figure 2. The GO sample has a planar-like, 2-D structure, while the B-rGO samples have a wrinkled undulated structure, which did not show much difference from the surface morphology of GO, other than that more corrugations were observed. The difference is due to the boron doping effect and deformation upon exfoliation in the carbon framework [23,50]. Similar observations have been reported by other researchers [2,42,51,52]. Also, boron-doping resulted in a decrease in the interlayer spacing (d_{002} spacing) of GO, as can be seen in Figure 2 (c) and (d).

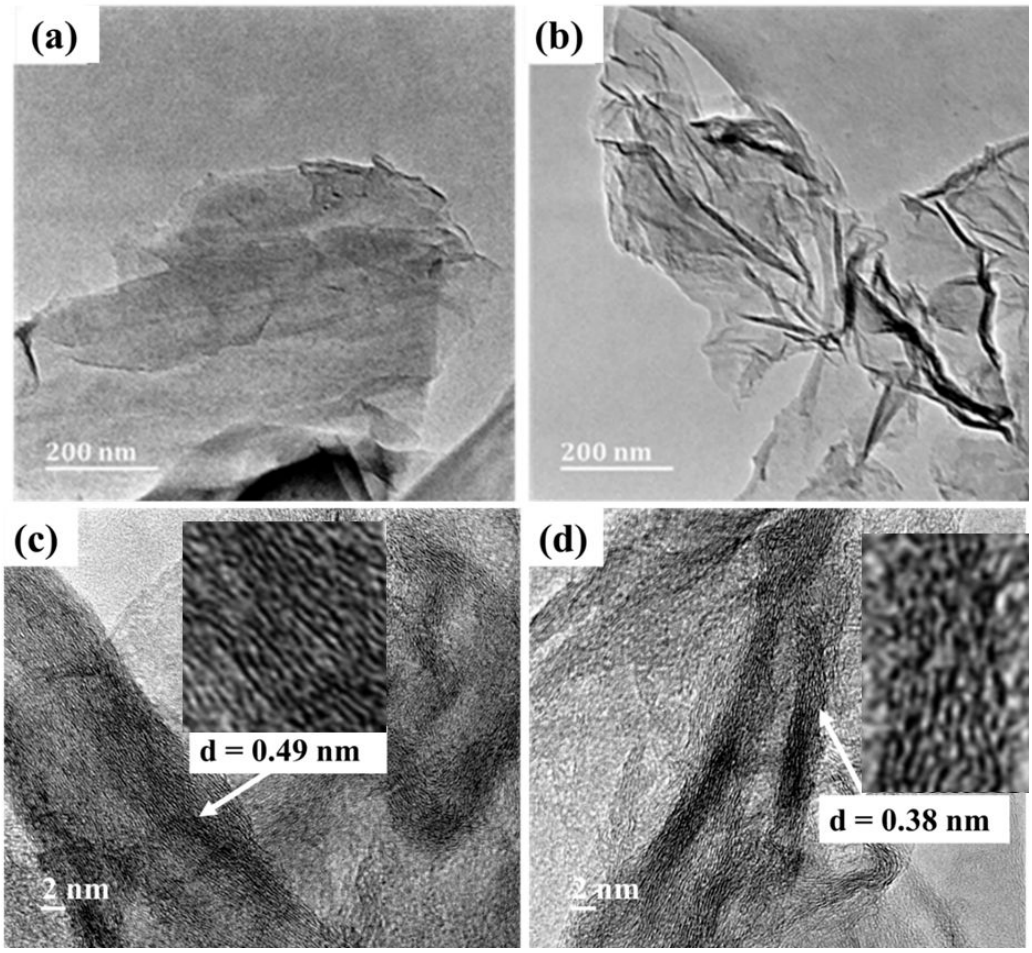

Figure 2: HR-TEM images of (a) GO and (b) B-rGO, and interlayer spacing of (c) GO and (d) B-rGO

Figure 3 shows SEM images of GO and various B-rGO samples. Images (b) to (e) reveal that the B-rGO samples contain randomly aggregated few-layers of ultra-fine sheets which are closely packed. A closer view shows that the nanosheets of B-rGO were randomly stacked together, displaying a flake-like structure. This was caused by the thermal annealing of GO and reduction of oxygen functional groups which resulted in a few fine layers of GO sheets [53]. Further structural properties of B-rGO samples were investigated by spectroscopic methods and are also discussed herein.

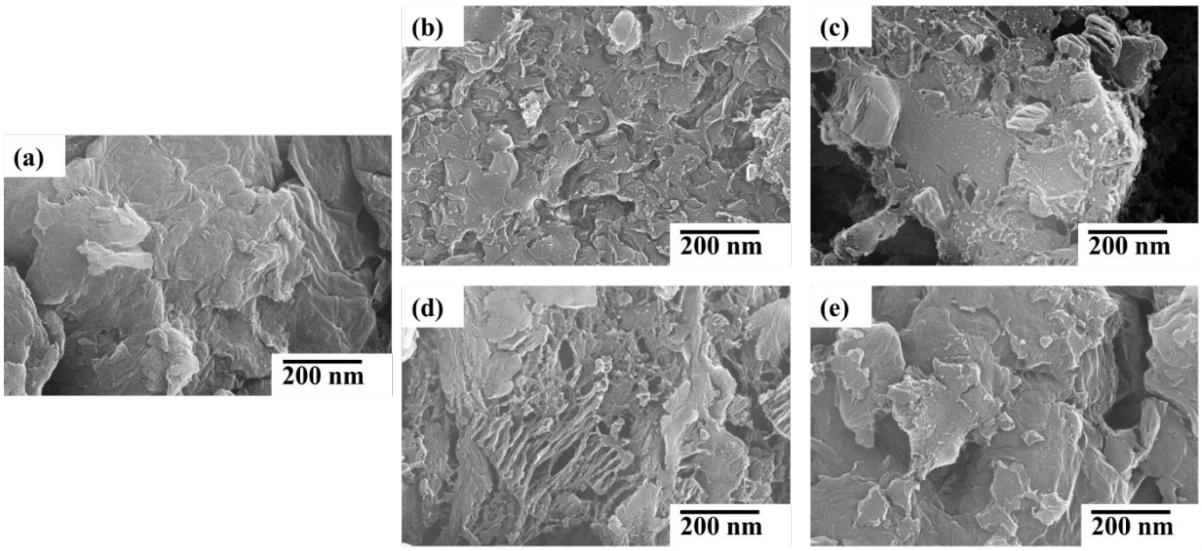

Figure 3: SEM images of (a) GO, (b) B-rGO-70, (c) B-rGO-60, (d) B-rGO-50 and (e) B-rGO-40

3.4 Crystallinity

Figure 4 (a) shows the Raman spectra of B-rGO which reveal the D- and G-bands at 1341 and 1592 cm^{-1}, respectively. The intensity of the D- and G-bands of B-rGO manifested a frequency down-shift compared with those of GO. The broadening of both D- and G-bands for B-rGO indicates the incorporation of the boron functional group and loss of crystalline nature [33,54]. In this work, an increase in intensity and broadening of the D-band was observed, which reveals a loss of crystallinity of B-rGO as the boron concentration increases. The ratio of I_D/I_G for the D- and G-bands was measured to deduce the disorder and defects present in the B-rGO samples [55] (see Table 2). Thus, the lower I_D/I_G ratio represents a higher degree of crystallinity while the higher I_D/I_G ratio suggests that the materials have a lower degree of crystallinity.

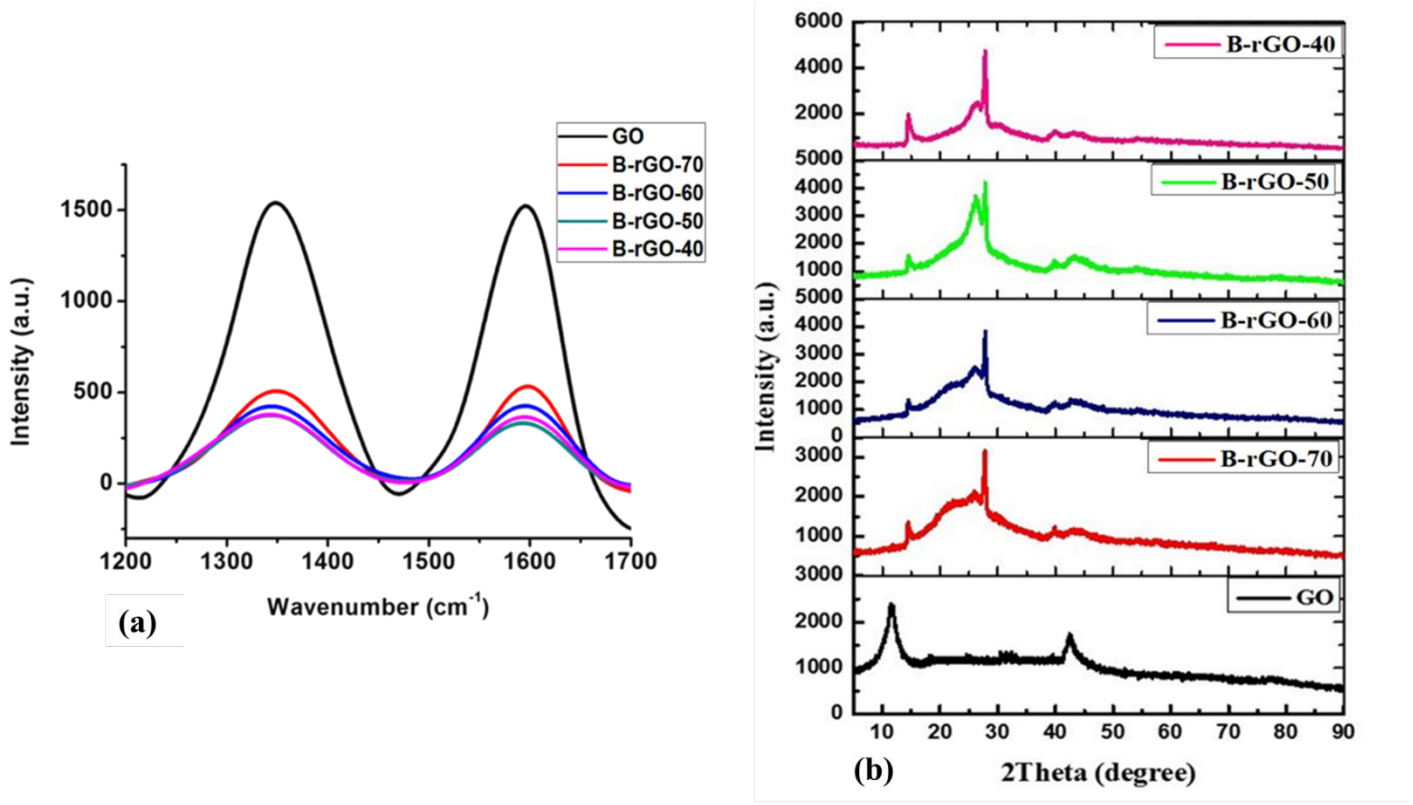

Figure 4: (a) Raman spectra and (b) Powder X-ray diffractograms of GO and B-rGO

As seen in Table 2, the I_D/I_G ratios for GO, B-rGO-70, B-rGO-60, B-rGO-50, and B-rGO-40 were 0.99, 1.33, 1.28, 1.26, and 1.23, respectively. The increment of the I_D/I_G ratio after boron-doping in GO has been reported by several researchers [33,35,56,57]. The increase in I_D/I_G ratio for B-rGO samples is attributed to a lower degree of crystallinity or disruption in the GO framework [58], which suggests the introduction of boron into the GO lattice and the introduction of more defects. The defects are due to boron-doping in the GO lattice and the harsh oxidation of graphite. The increase in boron concentration resulted in a higher I_D/I_G ratio, demonstrating the formation and increase in the amount of sp^3 hybridization and defects in the graphene sheet, which lead to changes in structural and electrical properties [59].

B-rGO-70 had the highest I_D/I_G ratio of 1.33 of all the B-rGO samples, due to its higher boron content. Also, the crystallite size (La) of B-rGO was observed to decrease with the increase in boron concentration (Table 2). The crystallite size was calculated with the use of an equation reported by Mallet-Ladeira et al. [60] given in Equation 1:

$$HWHM = 71 - 5.2\ La \qquad (1)$$

where *HWHM* represents the half-width at a half maximum which is half of the full width at half maximum (FWHM) when the function is symmetric. Further structural analysis of the B-rGO samples was performed by powder-XRD.

Table 2: Crystallinity of GO and B-rGO

Sample	**D-band/± 1 cm^{-1}**	**G-band/± 1 cm^{-1}**	**I_D/I_G**	**La/nm**
GO	1350	1590	0.99	4.44
B-rGO-70	1348	1594	1.33	3.31
B-rGO-60	1345	1593	1.28	3.43
B-rGO-50	1342	1591	1.26	3.49
B-rGO-40	1341	1592	1.23	3.58

The diffractograms of the GO and B-rGO samples exhibited graphitic diffraction patterns which are shown in Figure 4 (b). GO showed a strong peak at a 2θ angle of 11° (d = 0.770 nm) which is assigned to the non-functionalized GO [61]. The shift from 11° to 15° after boron doping suggests that oxygen functional groups were reduced in the occurrence of exfoliation with boron functionalities [33,41]. For B-rGO, the broad peaks were between 25° and 27° (d = 0.352 - 0.330 nm). The shift in 2θ peak (between 25 and 27°, corresponding to the (002) plane) to the left and its broadness demonstrated that the boron-doping resulted in a hexagonal crystal structure [15]. This broadening is attributed to stress, strain, and defects induced during boron-doping. This suggests that the B-rGO samples had a lower degree of crystallinity and graphitization. These results correlate with the Raman spectroscopy analysis (Table 2). The reduction of GO is caused by the use of 10% hydrogen in argon. During the reaction, hydrogen and oxygen are combined and form water and it is all blown-out of the exhaust pipe of the furnace, hence there will be less oxygen and more of reduced graphene oxide. The observed decrease in interlayer spacing is an additional indication that the boron atom has been successfully incorporated into the GO lattice [62], and this is consistent with HR-TEM studies, as seen in Figure 2 (c) and (d).

Table 3 shows the powder-XRD parameters (interlayer spacing and crystallite size) calculated from Scherrer's equation. An increase in boron content causes an increase in the structural strain of B-rGO samples by enhancing the surface defects of the graphite layer, which results

in broadening of the full width at half maximum (FWHM) of the peaks. This is an indication of a significant increase in the number of defects which is induced with an increase in the incorporation of the boron atom into the GO lattice. Also, the crystallite size (La) decreased from 2.97 to 0.64 nm with increasing boron content. Hence, based on the interlayer spacing and crystallite size calculations, the B-rGO-70 sample had the lowest degree of crystallinity or graphitization, and the smallest crystallite size.

Table 3: Powder-XRD-parameters of GO and B-rGO

Sample	2θ/degree	FWHM/β_{hkl}	Interlayer spacing/nm	Crystallite size (La)/nm
GO	11.5	2.81	0.770	2.97
B-rGO-70	25.3	13.2	0.352	0.64
B-rGO-60	25.4	11.0	0.350	0.77
B-rGO-50	25.9	7.74	0.344	1.11
B-rGO-40	26.9	6.88	0.330	1.24

3.5 Textural properties

The surface area and porosity of the B-rGO samples varied with boron content (Table 4). The boron-doping on the GO sheets tends to increase the surface area of B-rGO and this is due to the substitutional incorporation of boron atoms which provides defect-like small pores in the basal plane of the GO sheet, thereby inhibiting the formation of the graphitic structure [2]. The enhancement of surface area after boron-doping has been reported by Singh *et al.* [42], which was due to the open space between the two-dimensional nano-sheets. The increase in surface area and porosity with an increase in boron content as determined by the BET and BJH analysis respectively correlates with the results obtained from SEM images. However, when comparing the porosity and surface area of B-rGO, it is noted that both the pore volumes and surface area increase, whilst the pore sizes decrease, with increasing boron content. This is because of the defects created during boron-doping which lead to the weakening of the π-π interactions between the GO sheets and consequently change the structural morphology by forming more wrinkled and folded sheets [63].

Table 4: Textural characteristics of GO and B-rGO

Sample	Surface area/m^2 g^{-1}	Pore volume/cm^3 g	Pore size/nm
GO	55.00	0.2827	25.2
B-rGO-70	130.0	0.3710	5.20
B-rGO-60	84.13	0.2783	7.10
B-rGO-50	68.74	0.2032	13.8
B-rGO-40	64.61	0.1169	20.4

It is envisaged that boron-doping tends to create defects on the GO surface and also generates pores/holes resulting from the evolution of carbon dioxide and carbon monoxide during the thermal reduction treatment. This causes folding and crumpling of GO sheets due to their inherent smaller mechanical resistivity [64]. Therefore, the porous structure is increased by boron content. For example, Table 4 reveals that the B-rGO-70 sample had the largest BET-surface area and this was attributed to the greatest amount of boron in the sample and extra pores on the surface of GO, which is related to extra exfoliation and perforation on the GO sheets. On the other hand, the smaller surface area of B-rGO-40 may have been caused by the chemical reduction of GO which is associated with π-π stacking between rGO sheets, and this resulted in agglomeration [61]. The enhancement in agglomeration is due to Van der Waals forces from π-π interactions and is evident from the decrease in pore volume in B-rGO-40. The pore size was obtained from the spaces between GO sheets and it varied with boron content. Also, the pores observed for B-rGO samples were mesoporous, a phenomenon that can cause a fast charge-discharge process, known as ionic diffusion.

The adsorption isotherms of GO and B-rGO are typical type IV adsorption-desorption isotherms as seen in Supplementary data (Figure S2), and thus the samples are classified as type IV mesoporous materials with interconnected pore systems [65]. All samples exhibited H3-type hysteresis loops between ≈ 0.45 and 1.0 P/P_o with various sizes of cavitation. It was observed that cavitation increases with boron content and this type of hysteresis loop is characteristic of materials consisting of plate-like particles with slit-shaped pores. The observed hysteresis loops are consistent with the morphological structures observed in the SEM images.

3.6 Thermal stability

The thermal stability and purity of the samples as inferred from the TGA thermograms and derivatives weight are exhibited in Figure 5. The thermogram of GO demonstrates a succession of reaction steps due to the presence of diverse oxygen-containing functional groups (hydroxyl (C-OH), carbonyl (C=O), epoxide (C-O-C) and single-bonded oxygen (C-O)) [66,67]. However, after doping such reaction steps were not observed, evidencing that the reduction of oxygen-functional groups was successful. The thermograms showed the least amount of residual mass (4% weight) which in all cases was assigned to the presence of char.

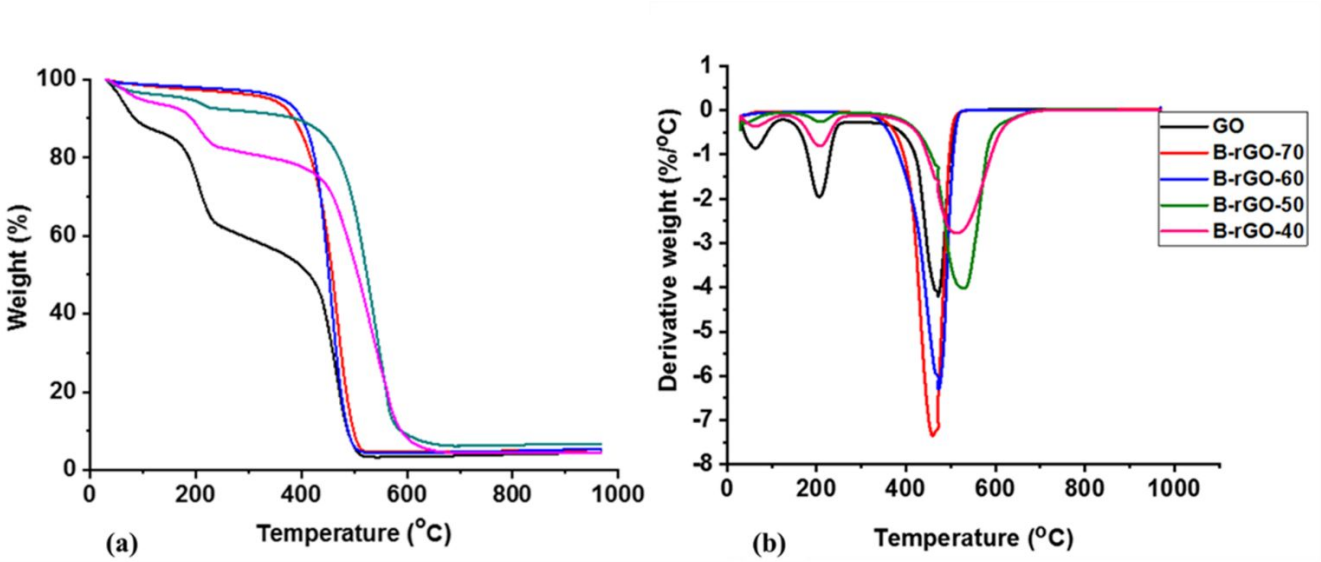

Figure 5: Thermal stability studies represented as (a) TGA thermograms and (b) derivatives weight for GO and B-rGO

The thermogram of GO showed a weight loss at 200 °C which was due to the loss of water and the removal of oxygen-containing groups in the sample (Figure 5). In contrast, the B-rGO-70 and B-rGO-60 samples did not show this weight loss. One major peak at 400 – 550 °C was observed for B-rGO and it showed the maximum decomposition temperature. The increase in the thermal stability of some B-rGO samples (B-rGO-40 and B-rGO-50) was observed after boron-doping. Duan *et al.* [68] demonstrated that doping graphene with a heteroatom can enhance the thermal stability of graphene. The heteroatom-doping sometimes tends to block the combustion sites and depress the formation of CO_x [69]. However, when comparing the B-rGO samples, the thermal stability decreases with an increase in boron content (Table 5), with B-rGO-70 being the least thermally stable. This was attributed to defects induced during

boron-doping, as supported by the observed TEM and SEM images where the B-rGO sheets were more folded. When nanomaterials are not crystalline, they are easy to break because they are not well-structured and this, results in a less stable material. The thermal stability of the B-rGO samples also correlates with their lower crystallinity as seen from the Raman spectroscopy analysis (Table 2).

Table 5: Decomposition temperatures of GO and B-rGO

Sample	Decomposition Temp./°C
GO	473
B-rGO-70	462
B-rGO-60	470
B-rGO-50	524
B-rGO-40	520

3.7 Optical properties

Figure 6 (a) shows the UV-Vis absorption spectra of B-rGO in the wavelength range of 200-800 nm. The synthesized GO exhibited a major absorption peak at 242 nm which is associated with a $\pi \rightarrow \pi^*$ electron transition in the C-C bonds [70,71]. The incorporation of boron resulted in an absorption shift from 275 to 303 nm. As the boron content increased, an enhanced electronic conjugation in the reduced B-rGO samples was observed.

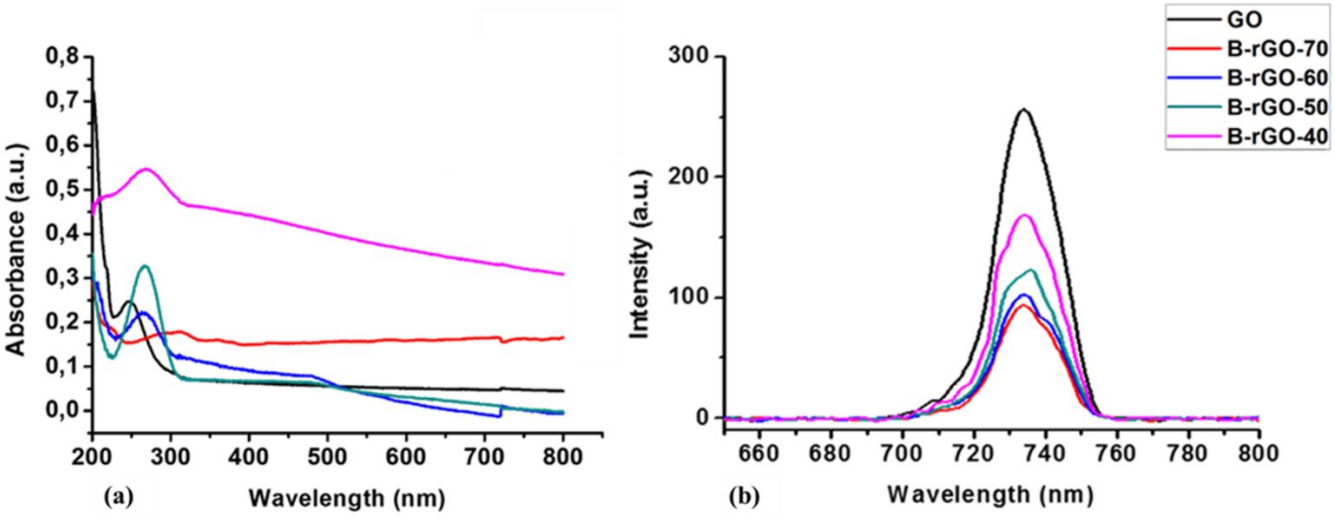

Figure 6: (a) UV-Vis absorption and (b) Photoluminescence spectra for GO and B-rGO

The bandgap energies for the nanomaterials were extrapolated from the Tauc's plot (Supplementary data – Figure S3) and are shown in Table 6. The *x*-axis intercept of the Tauc's plot to estimate the bandgap does not start at zero. Normally, the plot of $(\alpha h\nu)^2$ versus photon energy $(h\nu)$ gives a straight line in a certain region. The extrapolation of this straight line to the (hν)-axis gives the value of the indirect optical bandgap (E_g). In this case and according to the plots in the Supplementary data (Figure S3), tangents to the curves were drawn at linear segments to minimize the contribution of the phonons, and the intersection value (in eV) at the *x*-axis gives the direct bandgap energy according to Tauc's equation.

The absorption maxima in the UV-Vis absorption spectra of B-rGO are different because of the differences in the densities of state around the Fermi level and, thus, extrapolation in the Tauc's plots resulted in different bandgap values. The decrease in bandgap is a clear indication that the synthesized GO has been successfully reduced and doped with boron. Also, the decrease in bandgap energies resulted in the Fermi level moving up in the direction of the conduction band edge. The shift of the absorption edge or widening of the energy bandgap is due to the Moss-Burstein effect which originates from the lifting of the Fermi level into the conduction band potential because of the enhancement in the charge carrier concentration. It is also due to the decrease in shallow-level trap concentration close to the conduction band potential. It should be noted that the bandgap is dominated by π–π* and σ–σ* interband transitions, generally represented as E_g σ–σ*(E_g π–π*), however, the contributions arising from the Penn gap E_o σ–σ*(E_o π–π*) and broadening C σ–σ*(C π–π*) affects the expected shift in the presence of the "hole" imposing dopant, due to the enhanced transition of π-electrons (in p_z-type orbitals) to π* anti-bonding states and, subsequently, to vacant orbitals in boron. This phenomenon can be argued to render electrons labile and susceptible external field effects.

Table 6: Energy bandgaps of GO and B-rGO

Sample	**λ_{max} absorption/nm**	**Bandgap energy/eV**
GO	242	3.9
B-rGO-70	303	2.5
B-rGO-60	275	2.7
B-rGO-50	275	2.7
B-rGO-40	275	2.9

The variation in bandgap energy is due to the σ–σ* transition which comes from the σ–bonded electrons participating in the covalent bonds of both sp^3 and sp^2 carbon atoms. In a dopant environment, this determines electron oscillation strength S σ–σ* (S π–π*). However, the doping concentration and dopant configuration, as stated earlier, are varied and nonlinear. It can be argued that the observed trend arises from varied Tauc joined density of states and the classical Lorentzian dispersions in the neighbourhoods of the bandgap which is dependent on C- and B-hybridization in the B-rGO matrix. This is so because there is a strong correlation between the strength and the energy position of the oscillating electrons. Applying Tauc-Lorentz formalism becomes plausible because it averages the contributions of the π–π* and σ–σ* transitions resulting in energy values, which are not consistent with expected tight-binding molecular dynamics and are strongly correlated to the strength of electron binding energies.

To further investigate the optical properties, the band potentials were calculated by using the Butler and Ginley equations:

$$E_{VB} = X - E_e + 0.5\,E_g \quad (1)$$

$$E_{CB} = E_{VB} - E_g \quad (2)$$

where E_{VB} represents the valence band potential, E_{CB} represents the conduction band potential, E_g is the energy bandgap from (Table 6), X is the electronegativity of the semiconductor, and E_e is the energy of free electrons on the hydrogen scale (~ 4.5 eV). Table 7 shows the calculated band potentials of B-rGO. The values of $(\alpha h\nu)^2$ for $E < E_g$ appear non-zero due to intense multiple reflections from the film/substrate interface due to the low optical absorption originating from the weak π–π⋆ transition and at higher photon energy the optical absorption increases due to the major σ–σ⋆ transition. The change in the valence and conduction band potential after boron-doping was attributed to the Moss-Burstein effect. This is because of the high dopant concentration in B-rGO, thus the lower state of the conduction band is occupied by the excess electrons (carriers) from the boron (impurities) atoms, therefore the electrons require additional energy to be promoted from the valence band potential to the conduction band potential (empty state).

Table 7: Band potentials for GO and B-rGO

Sample	Valence band potential/eV	Conduction band potential/eV
GO	-1.66	-5.56
B-rGO-70	-2.74	-5.24
B-rGO-60	-2.64	-5.34
B-rGO-50	-2.64	-5.34
B-rGO-40	-2.59	-5.39

It is not possible to consider flat band potentials in view of the varied dopant concentration and configuration, and thus the change in conduction band potential is subject to the density of states and dispersion around the Fermi level. The conduction band of B-rGO-40 is greater due to more movement of partially filled electrons. Thus, it has a greater energy level. The valence band potential value for B-rGO-70 is greater because of the π-state which disappears near the Fermi level due to bonding between the π- and boron-related state, causing electron transfer from graphene to boron. Boron-doping tended to enhance the valence band potential of GO and a new hybridized band was formed between -2.24 and -2.74 eV under the Dirac point. This affected the energy state of adjacent bands which gave rise to charge redistribution. As a result, an electric charge, equivalent but opposite in sign to the charge, captured at the surface state, was generated inside B-rGO, leading to the formation of a space charge layer near the surface. The thickness of the space charge layer increased with decreasing concentration of the mobile charge carriers, and this was observed with increasing boron concentration. Thus, the work function of GO can be altered or tuned just by varying the doping concentration of boron.

The charge separation rate of electron-hole (charge) recombination of B-rGO was investigated by means of photoluminescence spectroscopy. The photoluminescence spectra of the B-rGO samples at an excitation wavelength of 340 nm are shown in Figure 6 (b). It was observed that the intensity of the B-rGO peaks decreased drastically as compared with that of GO. This indicated that the electron-hole pair recombination has been successfully reduced with a prolonged lifetime of photogenerated carriers and this is due to the synergistic effect of B-rGO. B-rGO-70 with higher boron content tends to induce a lower rate of charge recombination as compared with the other samples that had lower boron content. These observations corroborate

the effect of varying boron content in B-rGO and the energy bandgap (Figure 6 (a)). However, there was no significant change in the photoluminescence spectra of the B-rGO and GO samples, indicating that the permissible excited states generally do not change.

3.8 Electrochemical properties

The current and resistance of B-rGO samples were measured with a four-point probe and, thus, the electrical conductivity (σ) and resistivity (ρ) could be determined at room temperature from the following equations:

$$\sigma = \frac{1}{\rho} \quad (3)$$

$$\rho = \frac{\pi\, h}{\ln 2}\left(\frac{\Delta V}{I}\right) \quad (4)$$

where h represents the thickness of the pellet, I is the current and ΔV represents the change in voltage. The values obtained are recorded in Table 8. The GO sample showed the highest resistivity, while the B-rGO samples exhibited much lower resistivities, due to the boron-doping effect. This was consistent with Poh *et al.* [72] who reported a similar decreasing trend in resistivity after doping graphene with boron.

Table 8: Electrical conductivity of GO and B-rGO

Sample	Sheet resistance/Ω sq^{-1}	Bulk resistivity/Ω cm	Electrical conductivity/S cm^{-1}
GO	2.415×10^{7}	2.188×10^{6}	4.570×10^{-7}
B-rGO-70	1.863×10^{1}	1.692×10^{-1}	5.920
B-rGO-60	3.100×10^{1}	2.810×10^{-1}	3.560
B-rGO-50	5.179×10^{1}	4.694×10^{-1}	2.135×10^{-1}
B-rGO-40	5.780×10^{3}	5.238×10^{1}	1.913×10^{-2}

The I–V characteristics of the B-rGO samples through basic conductivity estimations are shown in Figure 7. The I-V slope of GO was found to be close to zero, which implies that GO is an insulating material. The slight deviation of B-rGO-40 from a straight line demonstrated it is a non-Ohmic conductor. Increasing the boron content, produced a curved line passing

through the origin, which indicated that B-rGO-50, B-rGO-60 and B-rGO-70 have semiconductor field-effect characteristics. Thus, simultaneous reduction and doping of GO affords semi-conducting behavior. An increase in the I-V slope suggests that B-rGO has a higher electrical conductivity than GO. These results are in agreement with those reported by Van Khai *et al.* [73].

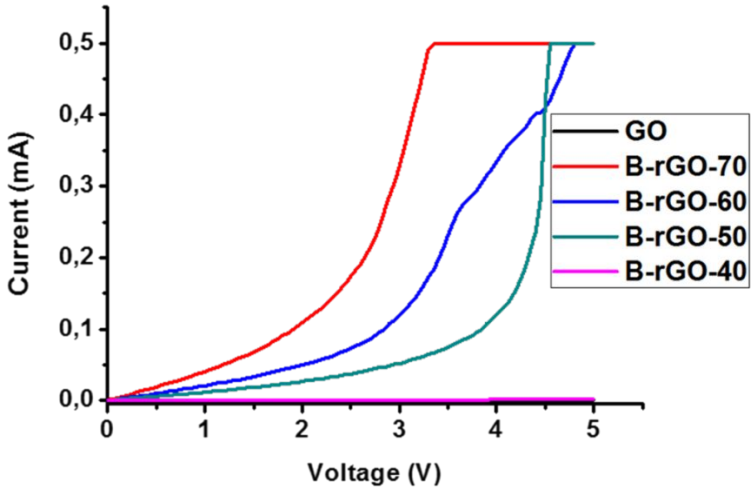

Figure 7: Current-voltage characteristics of GO and B-rGO

Among the B-rGO samples, B-rGO-70 was found to exhibit the largest conductivity, while B-rGO-40 showed the smallest conductivity. The enhancement in conductivity after doping with boron is caused by an increase in hole-type charge carriers in the GO network and is also due to the change of bonding configuration. It was seen that the conductivity increased with boron content in B-rGO, implying that all the B-rGO samples exhibited semi-conducting properties. These electrical conductivity behaviours are associated with the electron acceptor properties of the boron atom. From Figure 7, it can be deduced that B-rGO-40 showed a significant decrease in free carrier mobility, whilst the highest mobility of free carrier was in B-rGO-70. Based on the rigid band model, it can be inferred that the holes created and pore sizes on B-rGO-40 (BET results - Table 4) serve as a trap for free electrons. Thus, one can assume a decrease in free carrier mobility lowers the electrical conductivity. Generally, boron-doping caused a shift in the Fermi level away from the Dirac point (graphene) and resulted in a finite density of state at zero energy [74]. The Fermi level shift is highly dependent on the doping concentration of boron atoms. The finite density of state at zero energy is caused by the increase of quasi-particle weight in semi-conductors by impurity doping. Therefore, the electrical conductivity of B-

rGO is expected to increase when boron doping increases and is consistent with the electronic band structure (Table 7).

The Hall effect measurement results for carrier densities and mobilities of B-rGO are shown in Table 9. The trend in resistivity was determined from the Hall effect and it correlates with the trend of the resistivity obtained from the four-point probe measurements shown in Table 8. The Hall coefficient is negative which serves as an indication that all the B-rGO samples synthesized are *p*-type semiconductors. The carrier mobilities tended to vary with boron concentration for the B-rGO samples. B-rGO-70 manifested a *p*-type semiconducting behaviour with excellent carrier mobility (0.311 $cm^2\ V^{-1}\ s^{-1}$). Carrier mobility is a very important parameter for semiconductor materials. Higher mobility usually leads to better device performance. Graphene has been reported to have the highest carrier mobility among all the semiconductors because of the low effective mass. The high mobility of graphene-based materials can also stem from its one atom thickness in which the electron has a smaller scattering (due to its high confinement). Therefore, it is believed that the variation of boron content overcame the low conductivity of GO.

Table 9: Hall effect measurements for B-rGO at a constant field of 1160 G

Sample	Resistivity/Ω cm	Hall coefficient/$cm^3\ C^{-1}$	Carrier density/cm^{-3}	Carrier mobility/$cm^2\ V^{-1}\ s^{-1}$
B-rGO-70	0.2560	-0.0796	12.560	0.311
B-rGO-60	0.9691	-0.245	4.082	0.253
B-rGO-50	2.990	-0.323	3.096	0.108
B-rGO-40	5.806	-0.517	1.934	0.089

3.8.1 Electrode potential characteristics

Figure 8 (a) shows the CV curves for all the B-rGO samples over the optimized potential range. All the curves are almost quasi-rectangular in shape. The $[Fe(CN)6]^{3-/4-}$ redox probe current on GO was smaller than those of the B-rGO samples. Furthermore, the potential difference between the reduction and oxidation peaks of the $[Fe(CN)6]^{3-/4-}$ redox couple tends to decrease after boron-doping, due to the good electron transfer capability of B-rGO. All the B-rGO samples displayed good current responses and this was attributed to the different boron

functionalities present in B-rGO, which further enhanced semi-conductivity. B-rGO-40 shows pseudo-characteristics with a narrower rectangular shape than the other B-rGO samples. This is because of the switching of the current. It is deduced that a lower boron-doping concentration in GO presented some pseudo-characteristics and resulted in poor rate capacities. The redox current of the $[Fe(CN)6]^{3-/4-}$ redox probe was further enhanced with B-rGO-70. This further demonstrates that the variation of boron concentration effectively improved the electron transfer capability.

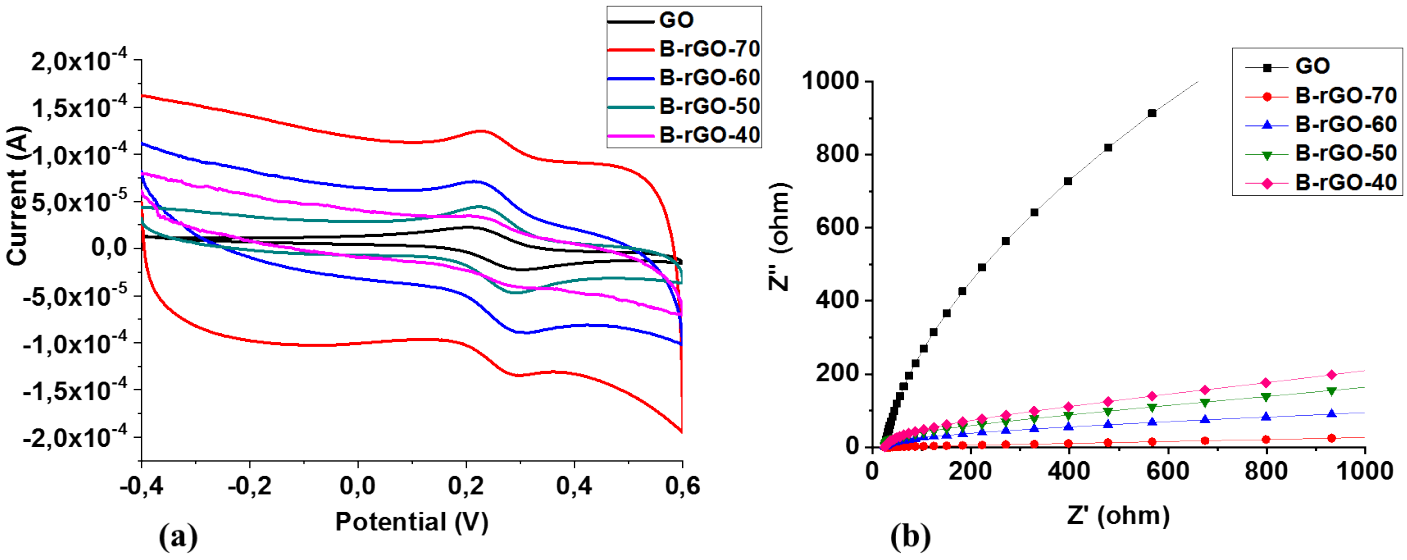

Figure 8: (a) Cyclic voltammograms curves and (b) Nyquist plots in the high-frequency region for GO and B-rGO samples

The high boron content in B-rGO-70 improved its capacitance which could be credited to an enhanced BET surface area (Table 4) and better electrical conductivity properties (Table 8). Consequently, the contribution through the electrochemical double-layer capacitance (EDLC) increased. The detailed mechanism of the Faradaic reaction is not yet understood in B-rGO. However, this pseudo-capacitive behaviour is due to the Faradaic redox reaction that is provided from the boron-containing enriched carbons [75]. Thus, improving the surface wetting by electrolytes enhances the electron capability. This concurs with other reports in that heteroatoms tend to cause an increment in the wettability of carbon-based electrodes and they enhance capacitance [2,76,77].

3.8.2 Interfacial charger transfer characteristics

In the Nyquist plot, GO shows a small semi-circle at the high-frequency region (Figure 8 (b)). However, after doping with various boron concentrations, the semi-circle disappears. This phenomenon is attributed to the mass transfer characteristics, which are predominant in the B-rGO samples, and corroborates the sharp increase in conductivity observed (Figure 7). In Figure 8 (b), the ascending order of slopes was B-rGO-70, B-rGO-60, B-rGO-50, B-rGO-40, and GO. This demonstrates that B-rGO-70 has a lower mass flow than B-rGO-40. The lower mass flow is due to morphological and structural modification, and reduction of oxygen-containing functional groups. The low mass flow is very beneficial in energy storage devices due to its minimized energy wastage by reducing unwanted heat during charging and discharging processes.

A larger Faradaic charge transfer resistance (R_{ct}) was observed in GO (Table 10) due to the high number of oxygen-containing groups that lowers its electrochemical characteristics. After boron-doping, R_{ct} decreased in all of the B-rGO samples. Thus, increasing the boron concentration in B-rGO leads to a lower R_{ct}. B-rGO-70 exhibited the lowest R_{ct} of 20.23 Ω, which correlates to the absence of a semi-circle in the Nyquist plot. The lower R_{ct} suggests that B-rGO-70 has less charge transfer resistance than the other B-rGO samples. This further demonstrates that B-rGO-70 can be a better conductive material with a higher electron conduction network because of the synergistic effect. These results correlate with the trend in electrical conductivity properties of B-rGO (Table 8), making these materials more suitable for application in dye-sensitized solar cells as a counter electrode.

Table 10: Resistance values for GO and B-rGO obtained by fitting the impedance spectra

Sample	**R_{ct}/Ω**
GO	75.18
B-rGO-70	20.23
B-rGO-60	32.90
B-rGO-50	40.01
B-rGO-40	40.86

4. Conclusion

Boron atoms were successfully doped into the GO lattice at various boron concentrations. The boron content in B-rGO increased with boric anhydride concentration and reached its highest doping level of 7.12%, which imposed a significant change in the physicochemical, optical, electrochemical, and conductivity properties. B-rGO-70 had the largest BET surface area which enhanced the capacitance but also caused it to be the least thermally stable. B-rGO samples showed strong absorption in the ultraviolet region. The doped materials showed a significant difference in their electronic properties, suggesting that the greater the degree of boron doping in graphene, the greater is the conductivity. The chaotic surface morphology of B-rGO-70, with an open porous structure and a high surface area, tends to enhance its electrical conductivity. B-rGO-70 showed a typical semiconductor characteristic, with a sheet resistance of $1.863 \times 10^{1}\ \Omega\ sq^{-1}$. It also had the lowest R_{ct} of 20.23 Ω, which is an indicator of good electron transport through the electrode-electrolyte interface, which is a promising feature for the design and fabrication of electronic nanodevices.

Acknowledgments

The authors would like to thank the National Research Foundation (NRF, Grant numbers – 101357, 116505 and 103979), UKZN Nanotechnology Platform, Tertiary Education Support Programme (TESP) and the University of KwaZulu-Natal (UKZN) for facilities and financial support. The authors are grateful to Prof. Bice Martincigh and Dr. Edigar Muchuweni for proofreading the manuscript.

References

1. N. Chen, X. Huang and L. Qu, *Phys. Chem. Chem. Phys.*, 2015, **17**, 32077-32098.
2. D.-Y. Yeom, W. Jeon, N. D. K. Tu, S. Y. Yeo, S.-S. Lee, B. J. Sung, H. Chang, J. A. Lim and H. Kim, *Sci. Rep.*, 2015, **5**, 9811-9817.
3. L. Wang, Z. Sofer, P. Šimek, I. Tomandl and M. Pumera, *J. Phys. Chem. C*, 2013, **117**, 23251-23257.
4. S. Maharubin, X. Zhang, F. Zhu, H.-C. Zhang, G. Zhang and Y. Zhang, *J. Nanomater.*, 2016, **2016**, 6375962.
5. M.-L. Yang, N. Zhang, K.-Q. Lu and Y.-J. Xu, *Langmuir*, 2017, **33**, 3161-3169.
6. A. Omidvar, *Mater. Chem. Phys.*, 2017, **202**, 258-265.

7. N. Rohaizad, Z. Sofer and M. Pumera, *Electrochem. Commun.*, 2020, **112**, 106660.
8. S. M. Tan, H. L. Poh, Z. Sofer and M. Pumera, *Analyst*, 2013, **138**, 4885-4891.
9. Z. Zhai, H. Shen, J. Chen, X. Li and Y. Li, *ACS Appl. Mater. Interfaces*, 2020, **12**, 2805-2815.
10. L. Pan, Y. Que, H. Chen, D. Wang, J. Li, C. Shen, W. Xiao, S. Du, H. Gao and S. T. Pantelides, *Nano Lett.*, 2015, **15**, 6464-6468.
11. S. Agnoli and M. Favaro, *J. Mater. Chem. A*, 2016, **4**, 5002-5025.
12. L. Ferrighi and C. Di Valentin, *Surf. Sci.*, 2015, **634**, 68-75.
13. Y.-B. Tang, L.-C. Yin, Y. Yang, X.-H. Bo, Y.-L. Cao, H.-E. Wang, W.-J. Zhang, I. Bello, S.-T. Lee and H.-M. Cheng, *ACS Nano*, 2012, **6**, 1970-1978.
14. Z. Jia, Z. Zuo, Y. Yi, H. Liu, D. Li, Y. Li and Y. Li, *Nano Energy*, 2017, **33**, 343-349.
15. V. Thirumal, A. Pandurangan, R. Jayavel and R. Ilangovan, *Synth. Met.*, 2016, **220**, 524-532.
16. S. S. Samantaray, V. Sangeetha, S. Abinaya and S. Ramaprabhu, *Int. J. Hydrog. Energy*, 2018, **43**, 8018-8025.
17. Y. Liu, Z. Tai, J. Zhang, W. K. Pang, Q. Zhang, H. Feng, K. Konstantinov, Z. Guo and H. K. Liu, *Nat. Commun.*, 2018, **9**, 3641-3610.
18. S. Gong and Q. Wang, *J. Phys. Chem. C*, 2017, **121**, 24418-24424.
19. X. Wu, Y. Wang and P. Yang, *Phys. Lett. A*, 2017, **381**, 2004-2009.
20. R. Lv, G. Chen, Q. Li, A. McCreary, A. Botello-Méndez, S. Morozov, L. Liang, X. Declerck, N. Perea-López and D. A. Cullen, *Proc. Natl. Acad. Sci. USA*, 2015, **112**, 14527-14532.
21. W. Cheng, X. Liu, N. Li, J. Han, S. Li and S. Yu, *RSC Adv.*, 2018, **8**, 11222-11229.
22. T. Zhang, H. Zhao, G. Fan, Y. Li, L. Li and X. Quan, *Electrochim. Acta*, 2016, **190**, 1150-1158.
23. H. Fang, C. Yu, T. Ma and J. Qiu, *Chem. Commun.*, 2014, **50**, 3328-3330.
24. A. J. Du, S. C. Smith and G. Q. Lu, *Chem. Phys. Lett.*, 2007, **447**, 181-186.
25. L. Tsetseris and S. T. Pantelides, *Carbon*, 2014, **67**, 58-63.
26. T. M. Dieb, Z. Hou and K. Tsuda, *J. Chem. Phys.*, 2018, **148**, 241716-241717.
27. I. Pletikosić, M. Kralj, P. Pervan, R. Brako, J. Coraux, A. N'diaye, C. Busse and T. Michely, *Phys. Rev. Lett.*, 2009, **102**, 056808.
28. P. Rani and V. Jindal, *RSC Adv.*, 2013, **3**, 802-812.
29. V. Barone, O. Hod and E. G. Scuseria, *Nano Lett.*, 2006, **6**, 2748 - 2754.

30. R. Q. Wu, L. Liu, G. W. Peng and Y. P. Feng, *Appl. Phys. Lett.*, 2005, **86**, 122510-122513.
31. Y. W. Son, M. L. Cohen and S. G. Louie, *Phys. Rev. Lett.*, 2006, **97**, 216801-216804.
32. B. Quan, S.-H. Yu, D. Y. Chung, A. Jin, J. H. Park, Y.-E. Sung and Y. Piao, *Sci. Rep.*, 2014, **4**, 5631-5636.
33. M. Mannan, Y. Hirano, A. Quitain, M. Koinuma and T. Kida, *J. Mater. Sci. Eng.*, 2018, **7**, 492-496.
34. J. Borowiec and J. Zhang, *J. Electrochem. Soc.*, 2015, **162**, B332-B336.
35. E. Romani, D. Larrude, M. da Costa, G. Mariotto and F. Freire, *J. Nanomater.*, 2017, **2017**, 1-8.
36. S. Li, Z. Wang, H. Jiang, L. Zhang, J. Ren, M. Zheng, L. Dong and L. Sun, *Chem. Commun.*, 2016, **52**, 10988-10991.
37. R. A. Thearle, N. M. Latiff, Z. Sofer, V. Mazánek and M. Pumera, *Electroanalysis*, 2017, **29**, 45-50.
38. L. Wang, Z. Sofer, J. Luxa and M. Pumera, *J. Mater. Chem. C*, 2014, **2**, 2887-2893.
39. S. Ge, J. He, C. Ma, J. Liu, F. Xi and X. Dong, *Talanta*, 2019, **199**, 581-589.
40. M. Sahoo, K. Sreena, B. Vinayan and S. Ramaprabhu, *Mater. Res. Bull.*, 2015, **61**, 383-390.
41. L. Panchakarla, K. Subrahmanyam, S. Saha, A. Govindaraj, H. Krishnamurthy, U. Waghmare and C. Rao, *Adv. Mater.*, 2009, **21**, 4726-4730.
42. M. Singh, S. Kaushal, P. Singh and J. Sharma, *J. Photochemi. Photobiol. A Chem.*, 2018, **364**, 130-139.
43. Z.-H. Sheng, H.-L. Gao, W.-J. Bao, F.-B. Wang and X.-H. Xia, *J. Mater. Chem.*, 2012, **22**, 390-395.
44. W. S. Hummers Jr and R. E. Offeman, *J. Am. Chem. Soc.*, 1958, **80**, 1339-1339.
45. H. Yu, B. Zhang, C. Bulin, R. Li and R. Xing, *Sci. Rep.*, 2016, **6**, 36141-36147.
46. P. Ranjan, S. Agrawal, A. Sinha, T. R. Rao, J. Balakrishnan and A. D. Thakur, *Sci. Rep.*, 2018, **8**, 12001-12013.
47. N. I. Zaaba, K. L. Foo, U. Hashim, S. J. Tan, W.-W. Liu and C. H. Voon, *Procedia Eng.*, 2017, **184**, 469-477.
48. X. Mu, B. Yuan, X. Feng, S. Qiu, L. Song and Y. Hu, *RSC Adv.*, 2016, **6**, 105021-105029.
49. V. V. Chaban and O. V. Prezhdo, *Nanoscale*, 2016, **8**, 15521-15528.
50. Z.-S. Wu, W. Ren, L. Xu, F. Li and H.-M. Cheng, *ACS Nano*, 2011, **5**, 5463-5471.

51. F. Wu, Y. Xing, L. Li, J. Qian, W. Qu, J. Wen, D. Miller, Y. Ye, R. Chen, K. Amine and J. Lu, *ACS Appl. Mater. Interfaces*, 2016, **8**, 23635-23645.
52. S. S. Balaji, M. Karnan, J. Kamarsamam and M. Sathish, *ChemElectroChem.*, 2019, **6**, 1492-1499.
53. A. T. Smith, A. M. LaChance, S. Zeng, B. Liu and L. Sun, *Nano Mater. Sci.*, 2019, **1**, 31-47.
54. Y. Hishiyama, H. Irumano, Y. Kaburagi and Y. Soneda, *Phys. Rev. B*, 2001, **63**, 245406-245411.
55. R. Beams, L. G. Cançado and L. Novotny, *J. Phys. Condens. Matter.*, 2015, **27**, 083002-083026.
56. S. Srivastava, S. K. Jain, G. Gupta, T. Senguttuvan and B. K. Gupta, *RSC Adv.*, 2020, **10**, 1007-1014.
57. Y. Bleu, F. Bourquard, V. Barnier, Y. Lefkir, S. Reynaud, A. S. Loir, F. Garrelie and C. Donnet, *Appl. Surf. Sci.*, 2020, **513**, 145843.
58. P. Han and A. Manthiram, *J. Power Sources*, 2017, **369**, 87-94.
59. L. G. Cançado, A. Jorio, E. M. Ferreira, F. Stavale, C. A. Achete, R. B. Capaz, M. V. d. O. Moutinho, A. Lombardo, T. Kulmala and A. C. Ferrari, *Nano Lett.*, 2011, **11**, 3190-3196.
60. P. Mallet-Ladeira, P. Puech, C. Toulouse, M. Cazayous, N. Ratel-Ramond, P. Weisbecker, G. L. Vignoles and M. Monthioux, *Carbon*, 2014, **80**, 629-639.
61. J. Zhang, H. Yang, G. Shen, P. Cheng, J. Zhang and S. Guo, *Chem. Comm.*, 2010, **46**, 1112-1114.
62. Y. Wang, C. Wang, Y. Wang, H. Liu and Z. Huang, *ACS Appl. Mater. Interfaces*, 2016, **8**, 18860-18866.
63. R. Nankya, J. Lee, D. O. Opar and H. Jung, *Appl. Surf. Sci.*, 2019, **489**, 552-559.
64. C.-M. Chen, J.-Q. Huang, Q. Zhang, W.-Z. Gong, Q.-H. Yang, M.-Z. Wang and Y.-G. Yang, *Carbon*, 2012, **50**, 659-667.
65. J. Lee, R. Nankya, A. Kim and H. Jung, *Electrochim. Acta*, 2018, **290**, 496-505.
66. F. Najafi and M. Rajabi, *Int. Nano Lett.*, 2015, **5**, 187-190.
67. J. Long, S. Li, J. Liang, Z. Wang and B. Liang, *Poly. Compos.*, 2019, **40**, 723-729.
68. X. Duan, S. Indrawirawan, H. Sun and S. Wang, *Catal. Today*, 2015, **249**, 184-191.
69. B. Frank, J. Zhang, R. Blume, R. Schlögl and D. S. Su, *Angew. Chem. Int. Ed.*, 2009, **48**, 6913-6917.

70. S. Schöche, N. Hong, M. Khorasaninejad, A. Ambrosio, E. Orabona, P. Maddalena and F. Capasso, *Appl. Surf. Sci.*, 2017, **421**, 778-782.
71. G. Jayalakshmi, K. Saravanan, B. Panigrahi, B. Sundaravel and M. Gupta, *Nanotechnology*, 2018, **29**, 185701-185722.
72. H. L. Poh, P. Šimek, Z. Sofer, I. Tomandl and M. Pumera, *J. Mater. Chem. A*, 2013, **1**, 13146-13153.
73. T. Van Khai, H. G. Na, D. S. Kwak, Y. J. Kwon, H. Ham, K. B. Shim and H. W. Kim, *Chem. Eng. J.*, 2012, **211**, 369-377.
74. H. Mousavi and R. Moradian, *Solid State Sci.*, 2011, **13**, 1459-1464.
75. J. Han, L. L. Zhang, S. Lee, J. Oh, K.-S. Lee, J. R. Potts, J. Ji, X. Zhao, R. S. Ruoff and S. Park, *ACS Nano*, 2012, **7**, 19-26.
76. J. Segalini, B. Daffos, P.-L. Taberna, Y. Gogotsi and P. Simon, *Electrochim. Acta*, 2010, **55**, 7489-7494.
77. R. Baronia, J. Goel, G. Gautam, D. Singh and S. K. Singhal, *J. Nanosci. Nanotechnol.*, 2019, **19**, 3832-3843.

Tuning the properties of boron-doped reduced graphene oxide by altering the boron content

Nonjabulo P. D. Ngidi, Moses A. Ollengo, and Vincent O. Nyamori*

School of Chemistry and Physics, University of KwaZulu-Natal, Westville Campus, Private Bag X54001, Durban 4000, South Africa

*Corresponding author: Tel. +27-31-2608256, Fax: +27-31-2603091, Email: nyamori@ukzn.ac.za

Email addresses of co-authors: nonjabulongidi@gmail.com, mosesollengo@gmail.com

Table of content

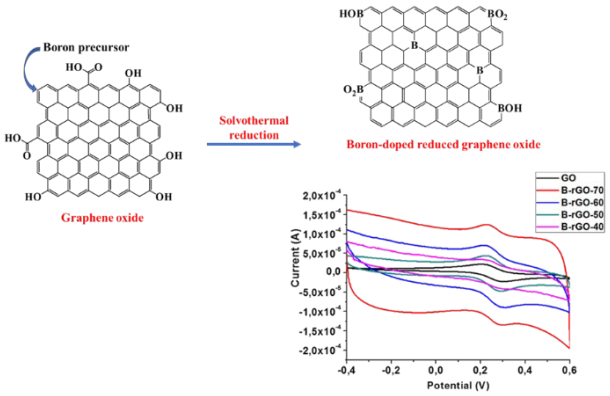

- Boron-doping enhanced the occurrence of the energy bandgap, the pore structure and interfacial charge transfer characteristics.